Analysis of the NaYF$_4$:Yb^{3+}, Er^{3+} nanocrystals: up-conversion luminescence, crystal structure and morphology influenced by the dopant concentration and annealing temperature

PEBETSI THOKWANE and PONTSHO MBULE*

Department of Physics, CSET, University of South Africa, Johannesburg 1710, South Africa
*Author for correspondence (mbuleps1@unisa.ac.za)

Abstract. NaYF$_4$:Yb^{3+},Er^{3+} nanocrystals were prepared using the combustion method. The samples were then annealed at 600 and 700°C for 2 h, respectively, to evaluate the effects of annealing temperature and the variation of the dopant concentration (Yb^{3+}-Er^{3+}). X-ray diffraction (XRD) analysis revealed the hexagonal phase (β-NaYF$_4$) for the as-prepared and the nanocrystals annealed at 600°C, as well as the cubic phase for the 700°C annealed nanocrystals. Scanning electron microscopy (SEM) images revealed a variety of morphologies, including spherical, cubic, hexagonal and porous particles, as dopant concentrations (10–30 mol% of Yb^{3+}, 1–3 mol% of Er^{3+}) and annealing temperatures were varied. Green and red up-conversion emission peaks centred at $\sim$483, 542 and 665 nm attributed to $^{2}H_{11/2} \rightarrow {}^{4}I_{15/2}$, $^{4}S_{3/2} \rightarrow {}^{4}I_{15/2}$ and $^{4}F_{9/2} \rightarrow {}^{4}I_{15/2}$ transitions of erbium, respectively, were observed under 980 nm laser excitation for all Yb^{3+}-Er^{3+} co-doped NaYF$_4$ nanocrystals. UV–Vis analysis revealed that the nanocrystals exhibit six characteristic peaks centred at $\sim$487, 520, 654, 802,972 and 1526 nm ascribed to $^{4}I_{15/2} \rightarrow {}^{4}F_{7/2}$ ($\sim$487 nm), $^{4}I_{15/2} \rightarrow {}^{4}H_{11/2}$ ($\sim$520 nm), $^{4}I_{15/2} \rightarrow {}^{2}F_{9/2}$ ($\sim$654 nm), $^{4}I_{15/2} \rightarrow {}^{4}I_{9/2}$ ($\sim$802 nm), $^{4}I_{15/2} \rightarrow {}^{4}I_{11/2}$ ($\sim$972) and $^{4}I_{15/2} \rightarrow {}^{4}I_{13/2}$ ($\sim$1500 nm) transitions of Er^{3+}, respectively. The absorption peak at $\sim$972 nm ascribed to the $^{2}F_{7/2}$ transition of Yb^{3+} overlaps with the $^{4}I_{11/2}$ absorption transition of Er^{3+}. Yb^{3+}-Er^{3+} doped NaYF$_4$ nanocrystals' up-conversion luminescence is studied for possible application in optical devices and solar cells.

Keywords. Up-conversion; luminescence; NaYF$_4$; combustion method; morphology.

1. Introduction

The potential of nanocrystals as a technological component for uses such as wavelength-tunable lasers, biosensing and photovoltaic cells may entirely depend on adjusting their behavioural patterns by incorporating impurities through doping [1]. Doping is an approach used to adjust nanocrystals to improve their electronic, luminescence and structural properties [2]. Doping inorganic nanocrystals with impurities like rare-earth (RE) ions achieves appealing outcomes because of their remarkable luminescence features [3]. Additionally, RE ion doping can be used to lengthen the life span of charge carriers and minimize the possibility of recombination [4]. RE ion-doped luminescent nanocrystals have drawn a lot of interest because of their potency for broad use in flat-panel showcases, solid-state sensors, photovoltaics, light-emitting peripherals, and particularly fluorescent labels for vulnerable biomolecule detection [5]. RE ions are incorporated in crystalline nanocrystals that are generally regarded as up-conversion nanocrystals, which are anti-stoke-type materials [6]. These nanocrystals have the capacity to refract light with long wavelengths into light with shorter wavelengths. Their emissions are based on an up-conversion process, in which two or more photons are successively absorbed, resulting in light emission at a shorter wavelength than the excitation wavelength. For example, near-infrared (NIR) or infrared light can be transformed into shorter-wavelength radiation, typically in the visible region of the electromagnetic spectrum [7,8]. During this process, one RE-dopant ion is given the energy of two or more IR photons, causing this ion to be excited into the 4f state at a high energy [7]. RE ions are incorporated in an inorganic matrix, resulting in prolonged luminescence lifetimes, high quantum efficiencies and photostability. The up-conversion of RE-doped inorganic nanocrystals takes place primarily in the host material's lattice and is largely unaffected by external environments [9]. Up-converting RE ions are incorporated into host materials such as oxides, oxysulphides and fluorides. These materials may combine numerous low-energy photons to create detectable higher-energy photons, making them appropriate for application in integrated optical devices such as planar optical amplifiers and low-cost NIR diodes, as well as solar cells. Because they can

lower multi-phonon non-radiative relaxation, materials with a low electron–hole recombination rate are regarded as the best hosts for RE ions for increasing up-conversion luminescence [10].

The photoluminescent characteristics of the trivalent RE-doped materials are influenced by the electrical intra-configurational *f–f* transitions of the RE ion. The intra-configurational transitions are mainly unaffected by the surrounding environment because the *4f*-orbitals of the RE ions are effectively insulated by the filled $5s^2 5p^6$ orbitals. In addition, unlike in semiconductor nanocrystals, instant particle size effects that affect electronic transitions, such as quantum confinement, cannot be observed in nanocrystals doped with trivalent RE ions. These effects are responsible for the fact that nanocrystals have a more ordered electronic structure. The luminescence dynamics of the trivalent RE ion, on the other hand, can be efficiently impacted by the particle size, surface, shape, strain and crystal phase of nanomaterials [11].

When compared to the properties possessed by other categories of luminescent materials, such as organic dyes or semiconductor dots, RE-doped materials possess remarkable photostability, high chemical robustness, and low toxicity. Because of the intra-configurational *f–f* electronic transitions, RE-doped fluorides also have narrow excitation and emission bands. In addition, the excited states have a longer duration (up to milliseconds), which allows for time-resolved detection to be possible. Time-resolved detection is extremely crucial for luminescence microscopy and biosensing [11]. Most lanthanide ions can achieve NIR-to-visible up-conversion; however, very efficient up-conversion is only possible with a few trivalent lanthanide ions (e.g., Er^{3+} and Tm^{3+}) when pump concentrations are low (980 nm excitation). So far, the Yb^{3+}-Er^{3+} or Yb^{3+}-Tm^{3+} co-doped sodium yttrium tetrafluoride ($NaYF_4$) nanocrystals are the most studied UC nanocrystals [12–14], and they are known to have the greatest luminescence qualities amongst all fluorescent materials [15], making them the best candidates for application in solar cells. $NaYF_4$ in the nanoscale size range is well-known as a very efficient host matrix for green and blue up-conversion, and $NaYF_4$:Yb^{3+}/Er^{3+} nanocrystals are mostly used in solar cells as photon absorption enhancers [10,13]. At room temperature, $NaYF_4$ nanocrystals exist in two polymorphs, namely, hexagonal and cubic, and are excellent luminous host matrices for UC due to their low phonon energy [10,15].

$NaYF_4$:Yb^{3+}, Er^{3+} up-conversion nanocrystals can be synthesized in several ways, including co-precipitation, hydrothermal, solvothermal processing, thermal decomposition, sol–gel, combustion and flame synthesis [16–18]. However, most of these synthesis methods require numerous complex steps that necessitate expensive equipment and precise experimental conditions. The advantage of combustion synthesis over other methods is that $NaYF_4$:Yb^{3+} and Er^{3+} nanocrystals can be prepared at a low cost. The combustion synthesis approach also allows the production of homogenous, crystalline, multi-component, fine powders at lower temperatures and with less production time. High reaction rates, on the other hand, frequently impair crystallinity and generate persistent contaminants that reduce brightness. To eradicate these incidences without causing excessive crystal development, an appropriate post-treatment is frequently necessary [19]. In 2016, Roh *et al* [20] successfully synthesized the $NaYF_4$:Yb^{3+}, Er^{3+} using a hydrothermal approach and incorporated them as an upconverting mesoporous layer onto $CH_3NH_3PbI_3$ perovskite solar cells (PSCs). The PSCs based on the upconverting mesoporous layer had a power conversion efficiency of 16.0%, an increase of 13.7% over traditional TiO_2 nanoparticle-based PSCs, owing to their NIR sunlight-capturing rate of 14.1%. This shows that hexagonal β-$NaYF_4$:Yb^{3+}, Er^{3+} nanoprisms increase photocurrent by broadening the absorption range of the PSC via up-conversion photoluminescence (PL). In 2018, Huang *et al* [21] used the thermal decomposition method to synthesize the core-shell $NaYF_4$:Yb^{3+}, Er^{3+} and $NaYF_4$ nanocrystals. The enhanced up-conversion luminescence of the produced nanoparticles under 980 nm stimulation is attributed to good surface defect suppression and the spatial isolation of doped ions.

The up-conversion characteristics of combustion-synthesized $NaYF_4$ nanocrystals doped with the Yb^{3+}-Er^{3+} pair at various relative concentrations to yield the highest up-conversion luminescence emission output are investigated in this work. Because Yb^{3+} has a very simple two-level energy system with one excited energy level $^2F_{5/2}$ around 980 nm and a larger and spectrally broader absorption cross-section than Er^{3+} [10], the UC luminescence performance can be improved by incorporating the Yb^{3+} ion as a sensitizer into Er^{3+} doped materials [22,23], where Yb^{3+} absorbs and transfers energy to Er^{3+} and emission occurs [16].

2. Experimental

2.1 *Materials*

The chemical reagents used in this study were of analytical grade and were used as received without any further purification from Sigma-Aldrich. Yttrium (iii) nitrate hexahydrate [$Y(NO_3)_3 \cdot 6H_2O$, 99.8%], sodium nitrate ($NaNO_3$, 99.0%), ammonium fluoride (NH_4F, 99.99%), urea (98%), ethanol (99.8%), erbium (iii) nitrate pentahydrate [$Er(NO_3)_3 \cdot 5H_2O$, 99.9%], and Ytterbium (iii) nitrate pentahydrate [$Yb(NO_3)_3 \cdot 5H_2O \geq 99.9\%$] were used as received. Urea was employed as a fuel because it increases the combustion rate and also undergoes a decomposition process that could contribute to the reduction of the combustion temperature.

2.2 *Combustion synthesis of NaYF₄ nanocrystals*

NaYF$_4$ nanocrystals were prepared using a combustion method, which involved dissolving 4.06 g of yttrium (III) nitrate hexahydrate [Y(NO$_3$)$_3$·6H$_2$O, 99.8%], 0.90 g sodium nitrate (NaNO$_3$, 99.0%), 1.57 g ammonium fluoride (NH$_4$F, 99.99%) and 2.08 g urea (98%) in 20 ml of ethanol. The clear solution was poured into a crucible and placed inside the furnace, which was preheated at 500°C for 20 min. After cooling to room temperature, the product was crushed into a fine powder with a mortar and pestle.

2.3 *Synthesis of Yb³⁺-Er³⁺ co-doped NaYF₄ nanocrystals*

For the preparation of Yb^{3+}-Er^{3+} co-doped NaYF$_4$ with various doping concentrations, stoichiometric amounts of ytterbium (iii) nitrate pentahydrate [Yb(NO$_3$)$_3$·5H$_2$O, ≥99.9%], erbium (iii) nitrate pentahydrate [Er(NO$_3$)$_3$·5H$_2$O, 99.9%], corresponding to 10, 20, 30 mol% (Yb^{3+}) and 1, 2, 3 mol% (Er^{3+}) doping levels were dissolved together with 4.06 g of Y(NO$_3$)$_3$·6H$_2$O, 0.92 g NaNO$_3$, 1.57 g NH$_4$F, and 2.08 g urea in 20 ml of ethanol with vigorous stirring at room temperature for 30 min. The clear solution was poured into a crucible and placed inside the furnace, which was preheated at 500°C for 20 min. After cooling to room temperature, the product was crushed into a fine powder with a mortar and pestle.

## 2.4 *Characterization of Yb³⁺-Er³⁺ co-doped NaYF₄ nanocrystals*

The crystallite phase of the produced nanocrystals was determined using an X-ray diffractometer (XRD; Cu K, 45 kV, and 200 mA) from the Rigaku SmartLab. Morphology was investigated using a JEOL JSM-7800 FESEM combined with an Oxford Aztec 350 X-Max 80 electron dispersive spectrometer (EDS). SHIMADZU-IRTracer-100 Fourier transform infrared spectroscopy (FTIR) spectra were acquired with a resolution of 4.0 cm^{-1} and 10 scans. The XploRA PLUS Raman microscope was used to observe the vibrational modes of molecules. A PerkinElmer Lambda 1050 UV/Vis/NIR spectrophotometer was used to quantify absorbance. The samples' up-conversion measurements were taken using a Horiba Jobin Yvon Fluorolog 3 Photoluminescence Spectrometer and a continuous LED laser beam with a wavelength of 980 nm. The thermal stability of the optimized NaYF$_4$:20%Yb^{3+}, 2%Er^{3+} sample was determined using the SDT (TGA) Q600 TA Instruments from room temperature to 700°C under a nitrogen flow rate of 60 ml min^{-1} and a heating rate of 10°C min^{-1}.

3. Results and discussion

3.1 *XRD analysis*

Figure 1a–c displays the XRD patterns of the as-prepared and annealed NaYF$_4$ and NaYF$_4$:Yb^{3+},Er^{3+} nanocrystals. The diffraction peaks of the as-prepared and annealed samples at 600°C closely matched the standard JCPDS data with card number 00-064-0156, indicating that the nanocrystals exhibit the hexagonal phase. The samples annealed at 700°C confirmed the formation of the cubic phase, matching well with the JCPDS data with card number 00-006-0342. The diffraction patterns of the nanocrystals revealed impurity peaks marked with an asterisk (*), which may have been caused by the rapid reaction times of the nanocrystals. Because of its high up-conversion quantum yield, hexagonal β-NaY$_{F4}$ is a more efficient host lattice for up-conversion PL for several lanthanide ions [20]. Some of the diffraction peaks vanished after the samples were annealed at 700°C. This could be due to the recrystallization of the material at high annealing temperatures, causing huge grain growth. Due to annealing, some of these grains are accumulated in one direction (preferred orientation) because of the recrystallization process. This indicates that the material's crystalline nature has changed. Either the phase dissolves in a multiphase combination or the phase has lost its crystalline nature and has become amorphous [24].

The dopant ionic radius influences the peak shift in the XRD peaks. If the dopant ionic radius is smaller than the base metal, it takes up an interstitial position, causing the lattice structure to shift and the d-spacing between the atoms to decrease. The diffraction peak shift was observed, as shown in figure 2a–c, for both as-prepared and annealed nanocrystals. The peak shift that was observed towards the lower and higher 2θ values is the result of the lattice expanding and contracting [25]. If the peak shift is in the direction of greater diffraction angles, this suggests that the crystal lattice is compressed, whereas a shift in the direction of lower diffraction angles shows that the crystal lattice is expanding [26]. In addition, peak-shifting occurs because of a continual change in the lattice constants as a function of composition [27]. Doping the NaYF$_4$ host leads the diffraction peaks to increase in intensity, broaden and shift. This is because when dopant atoms are introduced into the host structure, they replace some of the host atoms, causing the structure to shrink or expand. If the particles are of nanometre size, the diffraction peak will be extremely diffused and broad as the structure of the particles will be substantially reflected in their surface structure, which is highly disordered [28]. In addition, the shift of the diffraction peaks reflects an increase or decrease in the lattice parameters, owing mostly to the difference in ionic radii between the major elements and the dopant ions,
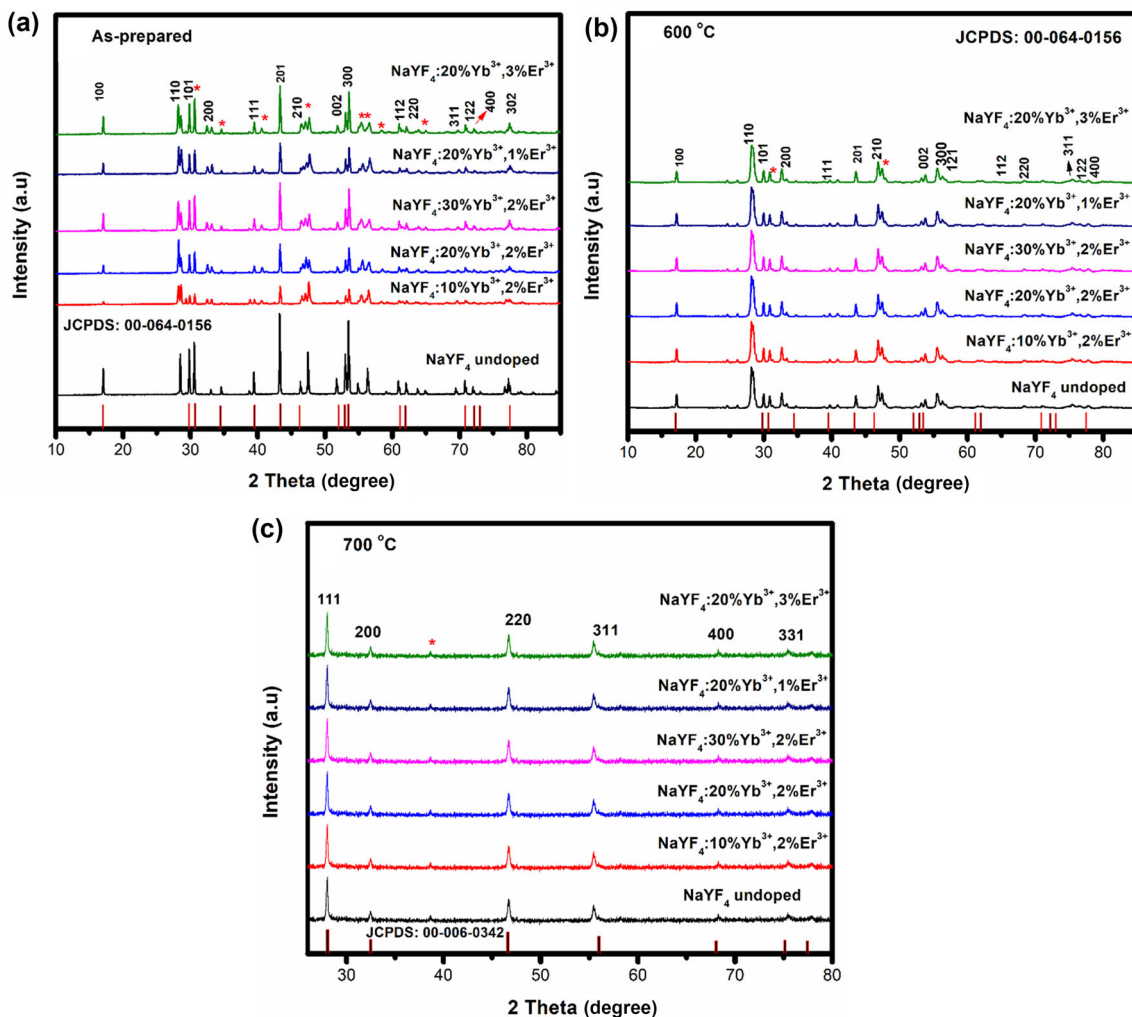
Figure 1. XRD patterns of Yb^{3+}-Er^{3+} co-doped NaYF$_4$ nanocrystals: (**a**) as-prepared, (**b**) annealed at 600°C, and (**c**) annealed at 700°C.

showing that the dopant ions have been successfully assimilated into the host lattice [29,30]. As a result of this peak shift, the lattice parameters were determined and summarized in table 1.

3.2 *Crystallite size, lattice parameters and strain analysis*

The Debye-Scherrer equation (1) [31] was used to compute the crystallite size of the samples, which uses the width of the peak at half of its greatest height (full-width at half-maximum, FWHM) of wide-angle X-ray scattering.

$$D = \frac{0.9\lambda}{\beta \cos\theta} \tag{1}$$

where λ is the X-ray source's wavelength, β the FWHM in radians, and θ the angle of Bragg's diffraction. The crystallite size, FWHM, lattice strain, and lattice parameters of the diffraction peak (100) for the as-prepared and nanocrystals annealed at 600°C and (220) for the nanocrystals annealed at 700°C were determined. The

crystallite size increased with an increase in Yb^{3+} concentration from 10 to 20% but decreased when the concentration was increased to 30%. When the Er^{3+} concentration was varied, the crystallite sizes of the nanocrystals decreased with the increase in Er^{3+} concentration. Moreover, the crystallite sizes of all the samples decreased with an increase in annealing temperatures. The lattice strains of the nanocrystals were estimated using equation (2) [32]:

$$\varepsilon = \frac{\beta}{4\tan\theta} \tag{2}$$

where ε is the lattice strain and β the FWHM. The lattice parameters for the cubic structures were determined using equation (3) [33]:

$$\frac{1}{d_{hkl}} = \frac{h^2}{a} + \frac{k^2}{b^2} + \frac{l^2}{c^2} \tag{3}$$

and for the hexagonal structures, the lattice parameters were determined using equation (4) [31]:
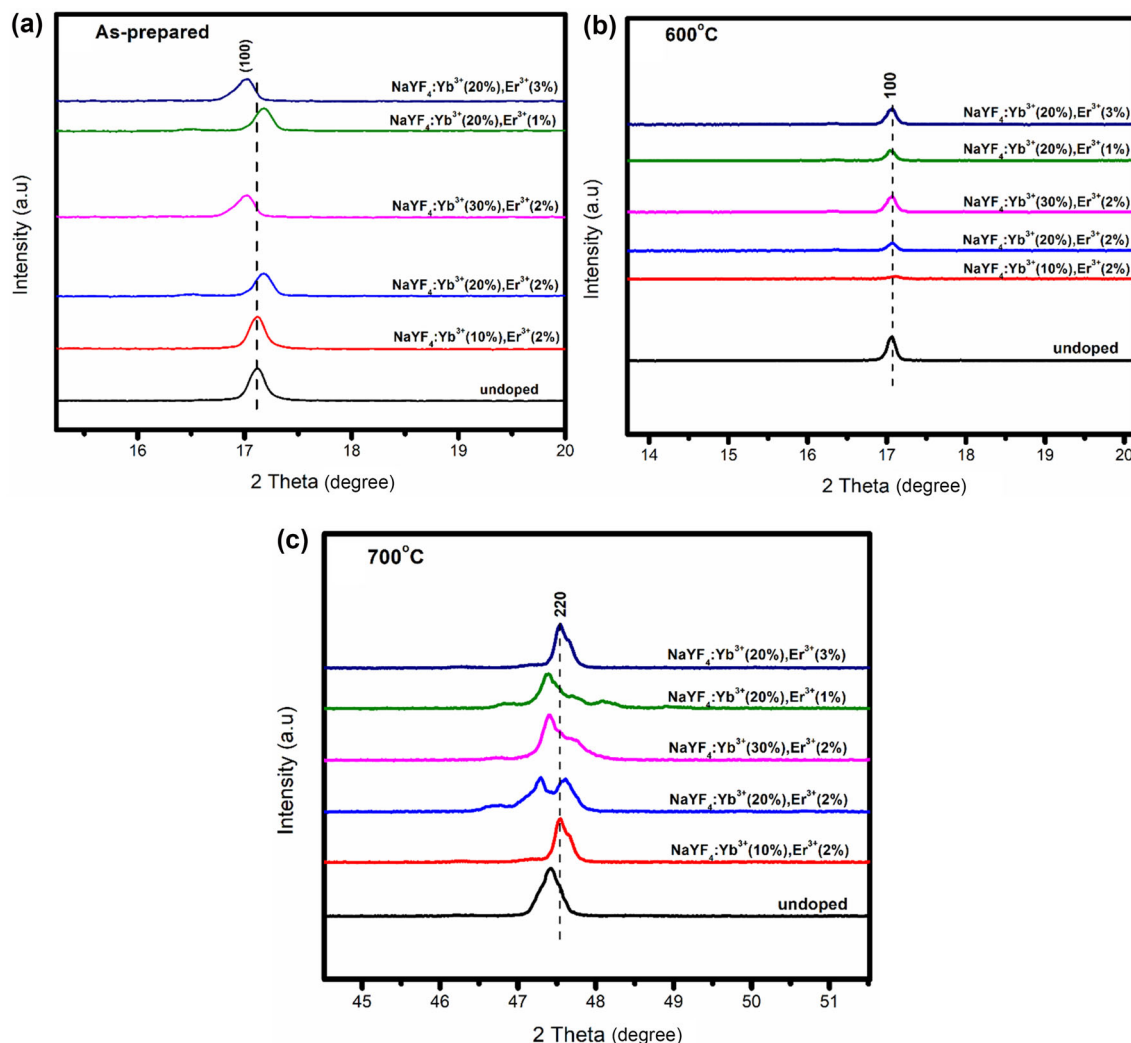
Figure 2. Diffraction peak shift analysis of Yb^{3+}-Er^{3+} co-doped $NaYF_4$ nanocrystals: (**a**) as-prepared, (**b**) annealed at 600°C and (**c**) annealed at 700°C.

$$\frac{1}{d_{hkl}} = \frac{4}{3}\left(\frac{h^2 + hk + k^2}{a^2}\right) + \frac{l^2}{c^2} \qquad (4)$$

where the interplanar spacing (d) was determined from equation (5) [32]:

$$2d_{hkl}\sin\theta = n\lambda_{cuk\alpha} \qquad (5)$$

The estimated crystallite sizes of the nanocrystals, lattice strains and lattice parameters are shown in table 1, and the relationships between the dopant concentrations and crystallite size and lattice strains are shown in figure 3a–d.

3.3 *FESEM and EDS and elemental mapping analysis*

The morphology of the nanocrystals was studied using the FESEM technique, as shown in figure 4a–f. The images of the undoped and Yb^{3+}-Er^{3+} co-doped $NaYF_4$ nanocrystals before annealing were captured. As it appears, the concentration of Er^{3+} ions was kept constant at 2 mol%, while the concentration of Yb^{3+} ions varied from 10 to 30 mol%. Again, the concentration of Yb^{3+} ions was kept constant at 20 mol%, while that of Er^{3+} ions was changed from 1 to 3 mol%.

In the process of varying the dopants' concentrations, the samples exhibited a dramatic difference in morphologies. Figure 4a shows spherical-like nanocrystals in undoped $NaYF_4$, whereas figure 4b and c shows that increasing the Yb^{3+} ion dopant concentration results in a combination of spherical-like and growing rod-like morphology. Figure 4d depicts a mixture of rods and cubic structures at the maximum Yb^{3+} doping concentration (30 mol%). On the other hand, when the Er^{3+} ion concentrations were changed from 1 to 3 mol% (as shown in figure 4c–f), the morphology changed to an irregular shape, then evolved into rods, and eventually the spherical morphology at the highest Er^{3+} ion concentration (3 mol%).

Table 1. Crystallite size, strain and lattice parameters at for Yb^{3+}-Er^{3+} co-doped $NaYF_4$ nanocrystals.

Sample name	2θ (^{o})	Crystallite size (nm)	Lattice strain ($\times 10^{-3}$)	Lattice parameters $a = b$ (Å)	Lattice parameters C (Å)
As-prepared samples					
$NaYF_4$ undoped	17.19	5.58	0.21	2.62	5.24
$NaYF_4$:Yb^{3+}(10%),Er^{3+}(2%)	17.19	7.25	0.16	2.62	5.24
$NaYF_4$:Yb^{3+}(20%),Er^{3+}(2%)	17.19	6.05	0.19	2.62	5.24
$NaYF_4$:Yb^{3+}(30%),Er^{3+}(2%)	17.19	5.18	0.23	2.62	5.24
$NaYF_4$:Yb^{3+}(20%),Er^{3+}(1%)	17.19	6.30	0.19	2.62	5.24
$NaYF_4$:Yb^{3+}(20%),Er^{3+}(3%)	17.19	5.18	0.22	2.62	5.24
Annealed at 600°C samples					
$NaYF_4$ undoped	17.19	4.84	0.24	2.62	5.24
$NaYF_4$:Yb^{3+}(10%),Er^{3+}(2%)	17.19	6.59	0.18	2.62	5.24
$NaYF_4$:Yb^{3+}(20%),Er^{3+}(2%)	17.19	5.80	0.20	2.62	5.24
$NaYF_4$:Yb^{3+}(30%),Er^{3+}(2%)	17.19	4.83	0.24	2.62	5.24
$NaYF_4$:Yb^{3+}(20%),Er^{3+}(1%)	17.19	5.37	0.22	2.62	5.24
$NaYF_4$:Yb^{3+}(20%),Er^{3+}(3%)	17.19	5.00	0.23	2.62	5.24
Annealed at 700°C samples					
$NaYF_4$ undoped	47.76	3.75	0.12	3.53	3.53
$NaYF_4$:Yb^{3+}(10%),Er^{3+}(2%)	47.76	5.15	0.09	3.53	3.53
$NaYF_4$:Yb^{3+}(20%),Er^{3+}(2%)	47.76	5.28	0.09	3.53	3.53
$NaYF_4$:Yb^{3+}(30%),Er^{3+}(2%)	47.76	5.03	0.09	3.53	3.53
$NaYF_4$:Yb^{3+}(20%),Er^{3+}(1%)	47.76	4.79	0.10	3.53	3.53
$NaYF_4$:Yb^{3+}(20%),Er^{3+}(3%)	47.76	5.03	0.10	3.53	3.53

Upon annealing the samples at 600°C, as shown in figure 5a–f), the undoped $NaYF_4$ nanocrystals displayed a highly agglomerated rod-like morphology (see figure 5a). Following that, hexagonally shaped morphologies were observed for $NaYF_4$: 10%Yb^{3+}, 2%Er^{3+} and $NaYF_4$: 20%Yb^{3+}, 2%Er^{3+}, as shown in figure 5b and c, with $NaYF_4$: 30%Yb^{3+}, 2%Er^{3+} exhibiting a clearer cubic-structured morphology in figure 5d. When the Er^{3+} ion concentration was increased from 1 to 3 mol% (as shown in figure 5c–f), the morphology evolved to an irregular particle shape with traces of spherical and hexagonal shapes at the Er^{3+} concentration of 3 mol%.

Figure 6a–f shows the samples annealed at 700°C. The undoped $NaYF_4$ and the doped samples where Yb^{3+} was varied (10–30 mol%) revealed the formation of a non-uniform morphology with pores. The observed pores are due to the gases escaping from the surface during the combustion process and the high annealing temperatures. When Er^{3+} was varied (1–3 mol%), the $NaYF_4$:20%-Yb^{3+},1%Er^{3+} sample showed a spherical morphology, whereas the $NaYF_4$:20%Yb^{3+},3%Er^{3+} sample showed a cubically structured morphology. All samples annealed at 700°C showed agglomeration of particles, which could be attributed to the high annealing temperature and weak magnetic interactions between the particles [34].

It can be deduced from these FESEM results that varying Yb^{3+} and Er^{3+} doping concentrations, as well as annealing temperatures, have a substantial effect on the morphology of $NaYF_4$ nanocrystals. As confirmed by XRD results, the crystal structure was greatly affected by the annealing temperatures, and this discovery is consistent with the FESEM results. EDS analysis was further conducted to evaluate the elemental composition of the prepared nanocrystals. As shown in figure 7a and b, expected elements like sodium (Na), yttrium (Y), fluorine (F), ytterbium (Yb) and erbium (Er) were confirmed. Oxygen detected from the EDS analysis might be from oxidation during the combustion process, while carbon might be from the carbon tape used to mount the powder samples. For both the undoped $NaYF_4$ and the Yb^{3+}-Er^{3+} co-doped $NaYF_4$, the corresponding elemental mappings of Na, Y, F, Yb and Er elements are shown in figure 8.

3.4 Photoluminescence analysis

Figure 9a and b depicts the up-conversion photoluminescence (UPL) emission spectra of the as-prepared $NaYF_4$ nanocrystals doped and co-doped with various concentrations of Yb^{3+} (10–30 mol%) and Er^{3+} (1–3 mol%) in the wavelength range from $\sim$400 to 800 nm under the excitation wavelength of 980 nm. All the samples showed the same spectra and the up-conversion luminescence phenomenon. The UPL emission spectra shows three significant emission bands at $\sim$483 nm (green light), $\sim$542 nm (green light) and $\sim$665 nm (red light), which are assigned to
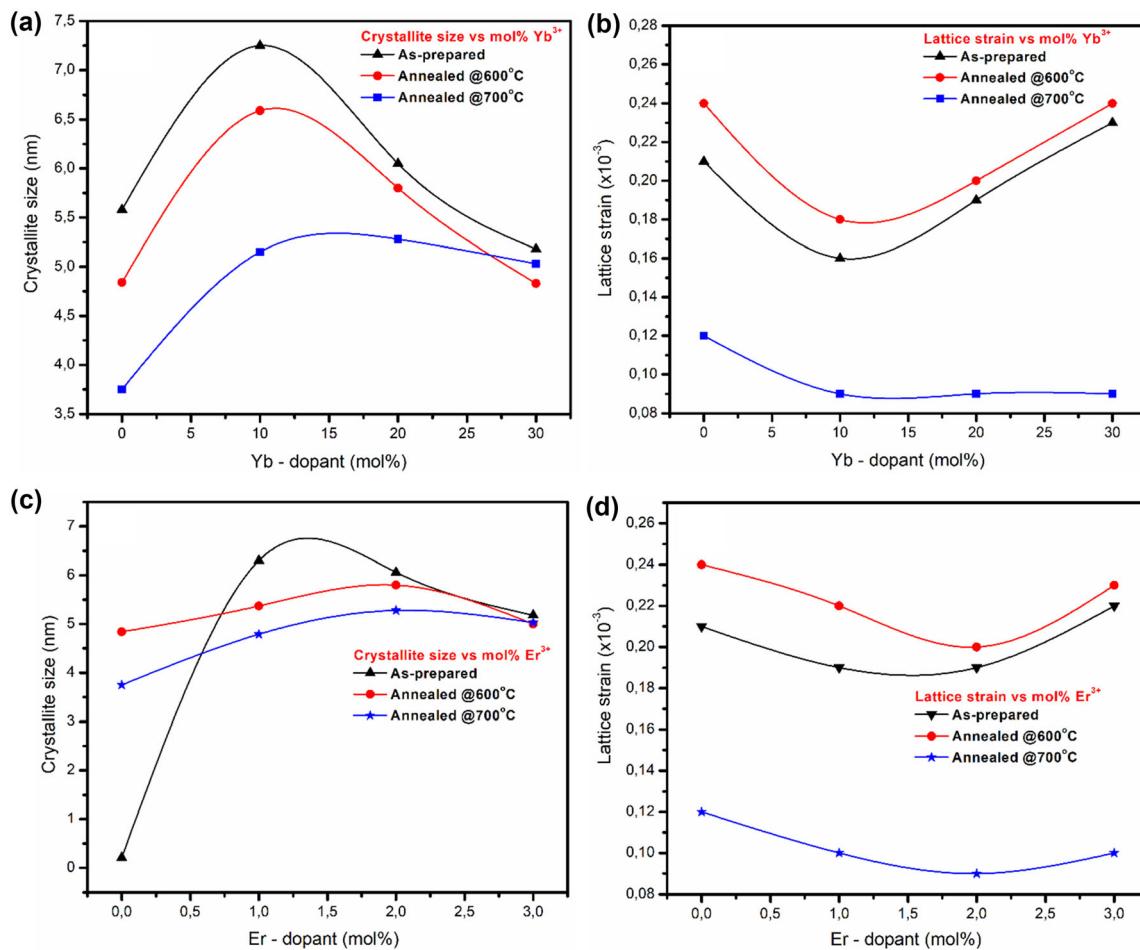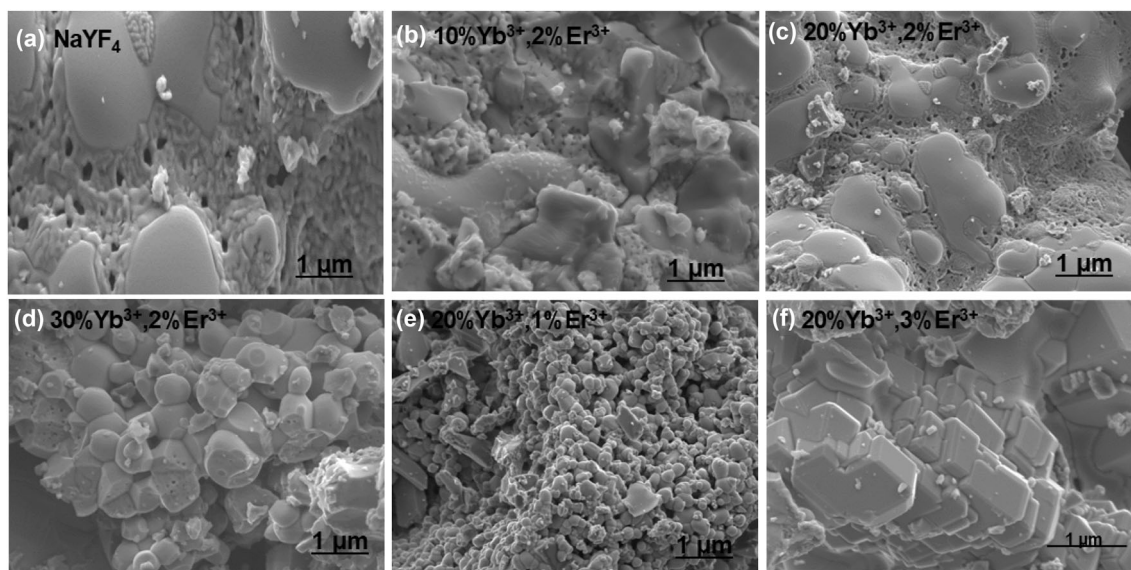
Figure 3. Relationship between the (**a**, **c**) crystallite size and (**b**, **d**) lattice strain *vs.* the Yb-Er-dopant concentrations.
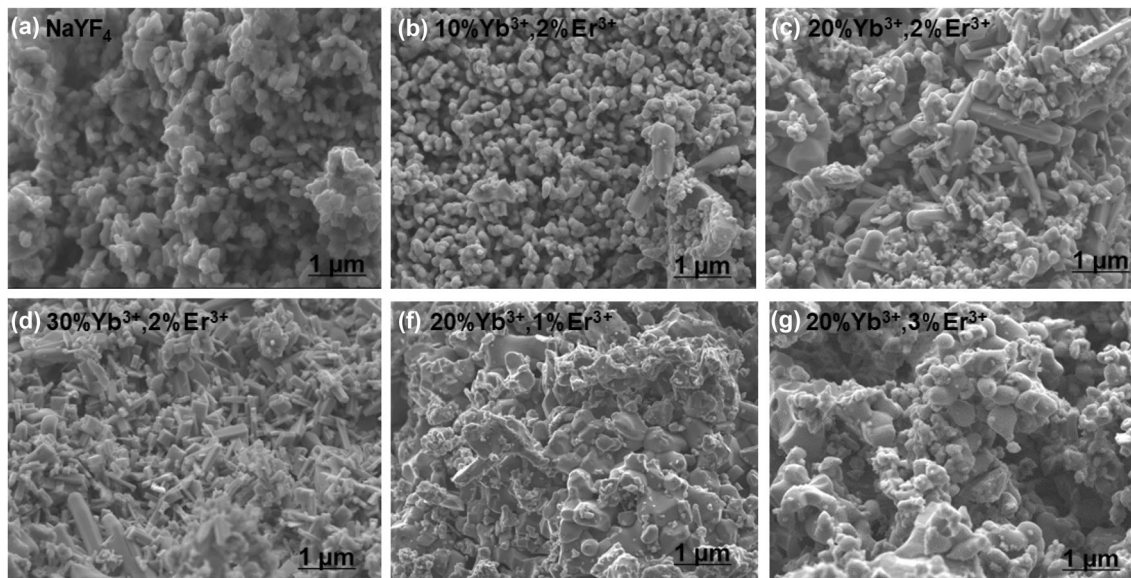
Figure 4. FESEM images of the undoped and Yb^{3+}–Er^{3+} co-doped $NaYF_4$ nanocrystals, before annealing.
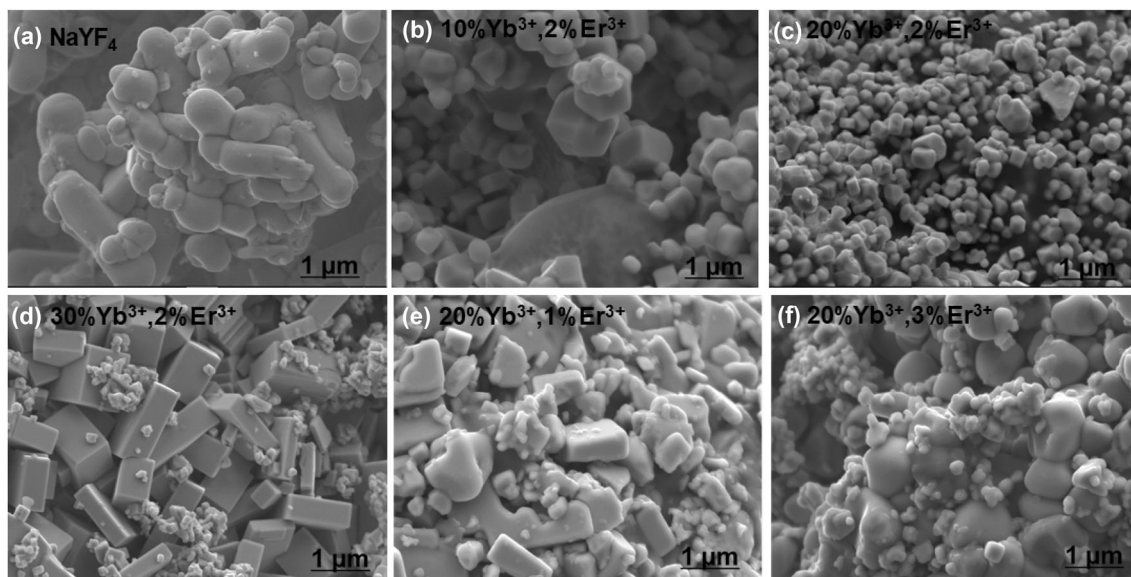
Figure 5. FESEM images of the undoped and Yb^{3+}–Er^{3+} co-doped $NaYF_4$ nanocrystals, annealed at 600°C.

Figure 6. FESEM images of the undoped and Yb^{3+}–Er^{3+} co-doped $NaYF_4$ nanocrystals, annealed at 700°C.

$^4H_{11/2} \rightarrow {}^4I_{15/2}$, $^4S_{3/2} \rightarrow {}^4I_{15/2}$ and $^4F_{9/2} \rightarrow {}^4I_{15/2}$ transitions of erbium, respectively [35,36]. It was observed that the increase in intensity of red emission is comparatively higher than green emission when the concentrations of Er and Yb are varied. To evaluate the influence of concentration on $NaYF_4$ up-conversion luminescence and the energy transfer mechanism, the sensitizer (Yb^{3+}) was varied from 10 to 30 mol% while the activator (Er^{3+}) was kept constant at 2 mol%. When the concentration of Yb^{3+} was increased from 10% to 20%, the luminescence intensity increased, showing the effective energy transfer from Yb^{3+} to Er^{3+} ions, but when the concentration was further increased to 30 mol%, the luminescence intensity decreased, demonstrating the concentration quenching effect. This may also be due to the

fact that increasing the doping concentration of dopant ions in nanocrystals increases the number of photon sensitizers and emitters, reduces the distance between the sensitizer and activator, and therefore boosts emission brightness. However, surpassing a concentration threshold may make the sequential energy transfer process less effective, as observed when Yb^{3+} concentration was increased to 30%, because concentration quenching dominates with high quantities of dopants. Hence, the ability to leverage the energy transfer process and, ultimately, their luminescence performance is governed by adequate doping concentration management in the particular host [37].

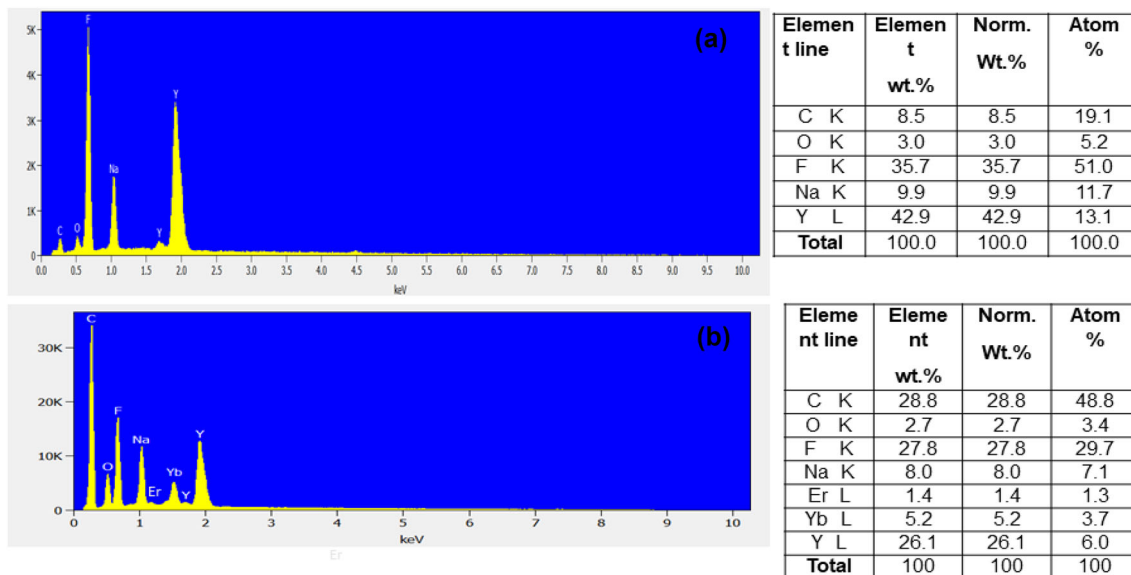To investigate the influence of temperature on the up-conversion luminescence of $NaYF_4$, the UPL for

Element line	Element wt.%	Norm. Wt.%	Atom %
C K	8.5	8.5	19.1
O K	3.0	3.0	5.2
F K	35.7	35.7	51.0
Na K	9.9	9.9	11.7
Y L	42.9	42.9	13.1
Total	100.0	100.0	100.0

Element line	Element wt.%	Norm. Wt.%	Atom %
C K	28.8	28.8	48.8
O K	2.7	2.7	3.4
F K	27.8	27.8	29.7
Na K	8.0	8.0	7.1
Er L	1.4	1.4	1.3
Yb L	5.2	5.2	3.7
Y L	26.1	26.1	6.0
Total	100	100	100

Figure 7. EDS spectra of the (**a**) undoped and (**b**) Yb^{3+}–Er^{3+} co-doped $NaYF_4$ nanocrystals.
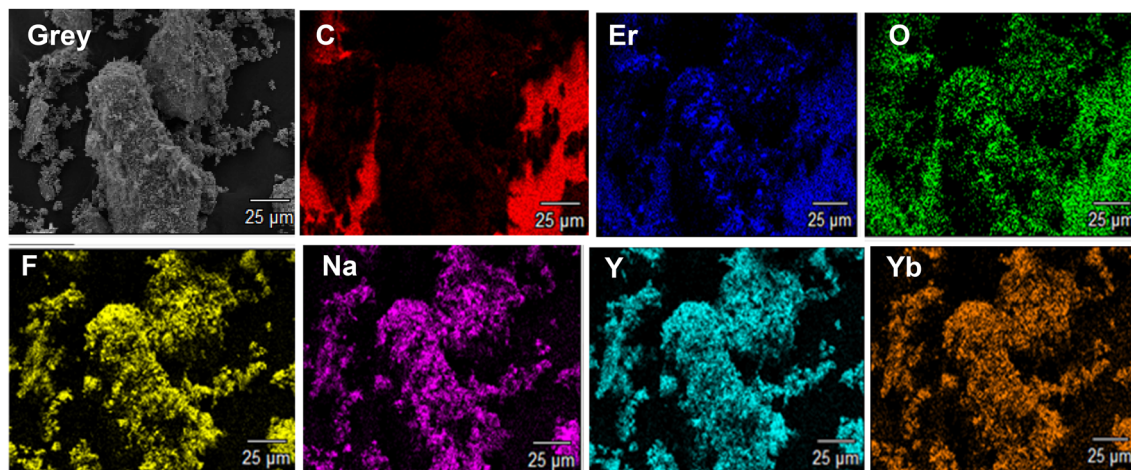
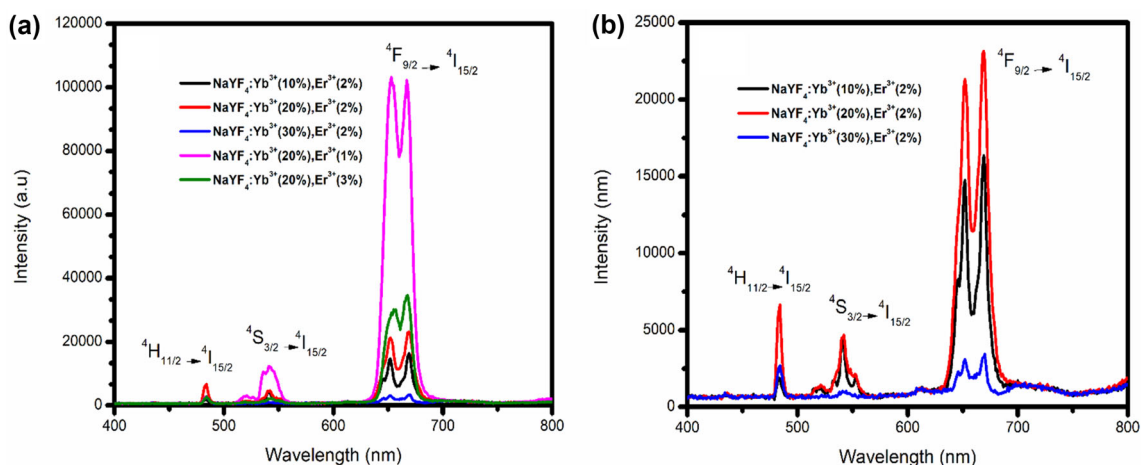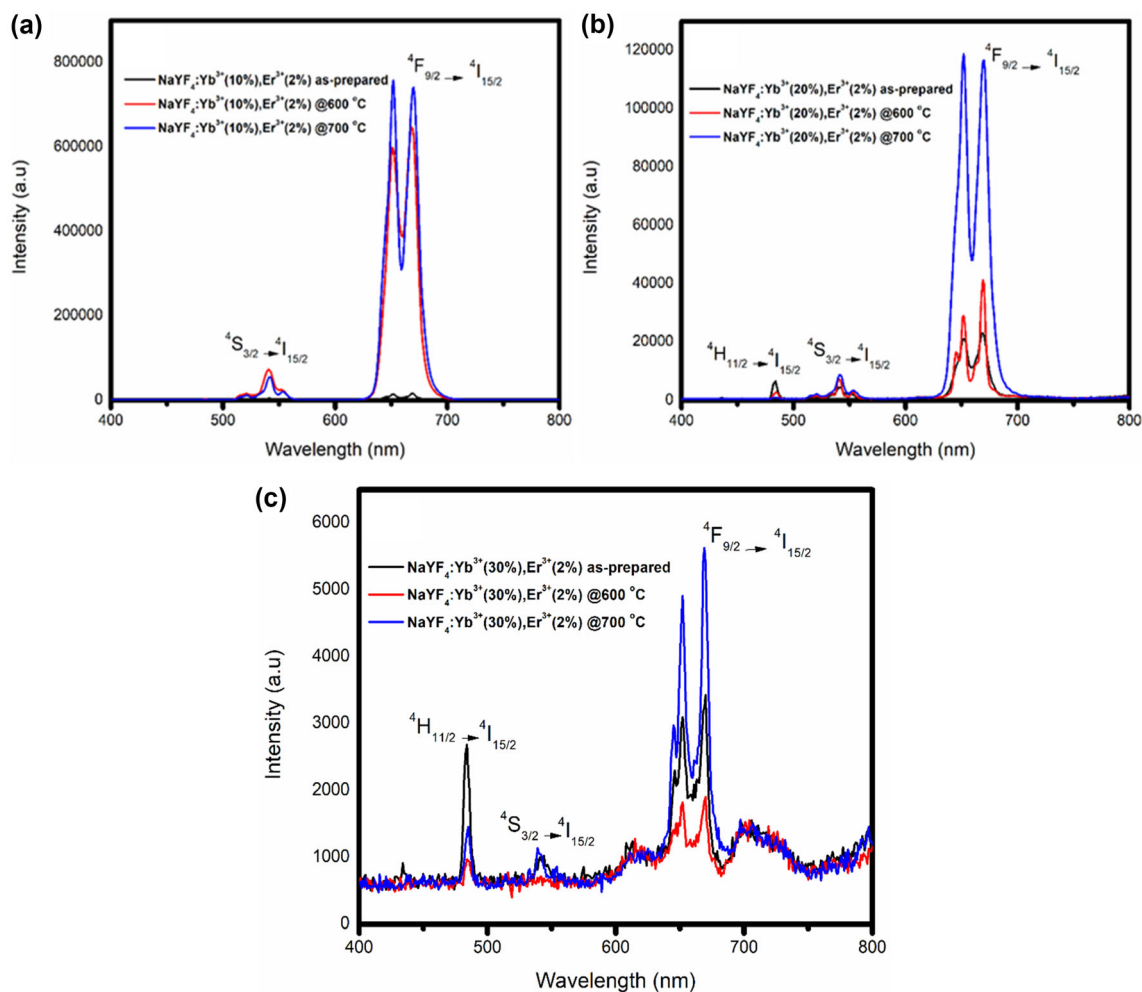**Figure 8.** Elemental mapping of the Yb^{3+}–Er^{3+} co-doped $NaYF_4$ nanocrystals.

Figure 9. Up-conversion emission spectra of Yb^{3+}-Er^{3+} co-doped $NaYF_4$ nanocrystals under laser beam excitation of 980 nm: (**a**) varying Yb^{3+} concentration and (**b**) varying Er^{3+} concentration.

Figure 10. Up-conversion PL spectra of (**a**) NaYF$_4$:10%Yb^{3+}, 2%Er^{3+}, (**b**) NaYF$_4$:20%Yb^{3+}, 2%Er^{3+} and (**c**) NaYF$_4$:30%Yb^{3+}, 2%Er^{3+}, showing the effects of annealing temperature on the luminescence intensity.

unannealed, annealed at 600 and 700°C NaYF4: x% Yb^{3+}, 2% Er^{3+} (x = 10, 20 and 30%) samples were plotted together and their intensities were compared (see figure 10a–c). The annealing of the nanocrystals enhanced the up-conversion luminescence. From these results, we observe that increasing concentrations of Yb^{3+} increase the luminescent intensity of the nanocrystals, but increasing the concentration above the concentration threshold reduces the UPL intensity of the nanocrystals due to concentration quenching, whereas increasing the annealing temperature enhances the PL intensity of the nanocrystals. Hence, the performance of the photoluminescent materials can be improved by carefully adjusting the annealing temperature and doping concentrations.

3.5 *UV–Vis analysis*

The UV–Vis absorption spectra and bandgap extrapolation of undoped NaYF$_4$ and Yb^{3+}-Er^{3+} co-doped nanocrystals are shown in figure 11a and b. Except for the undoped

NaYF$_4$, all samples exhibit the same trend, as shown in figure 11a. The absorption peak occurs in the 250–1800 nm wavelength range. The nanocrystals have six distinct Er^{3+} peaks at ∼487, 520, 654, 802, 972 and 1526 nm, which correspond to electron transitions of $^4I_{15/2} \rightarrow ^4F_{7/2}$ (∼487 nm), $^4I_{15/2} \rightarrow ^4H_{11/2}$ (∼520 nm), $^4I_{15/2} \rightarrow ^2F_{9/2}$ (∼654 nm), $^4I_{15/2} \rightarrow ^4I_{9/2}$ (∼802 nm) and $^4I_{15/2} \rightarrow ^4I_{13/2}$ (∼1500 nm), respectively. The absorption peak in the NIR wavelength range (∼972 nm) corresponds to the intense $^2F_{7/2}$ absorption band of Yb^{3+}, which overlaps with the $^4I_{11/2}$ absorption transition of Er^{3+}. The absorption spectra illustrates that both Er and Yb are well embedded into the lattice structure of NaYF$_4$ [38,39]. Optical absorption spectra are influenced by the shape, size, strain and vacancies in the samples. The red-shift seen in the optical absorption measurements, showing band gap shrinking, agrees with the drop in bandgap value with an increase in Er^{3+} dopant. The bandgap narrows when shallow donor impurities produce energy levels in the bandgap close to the conduction band edge and shallow acceptor impurities produce energy levels close to the valence band edge. The
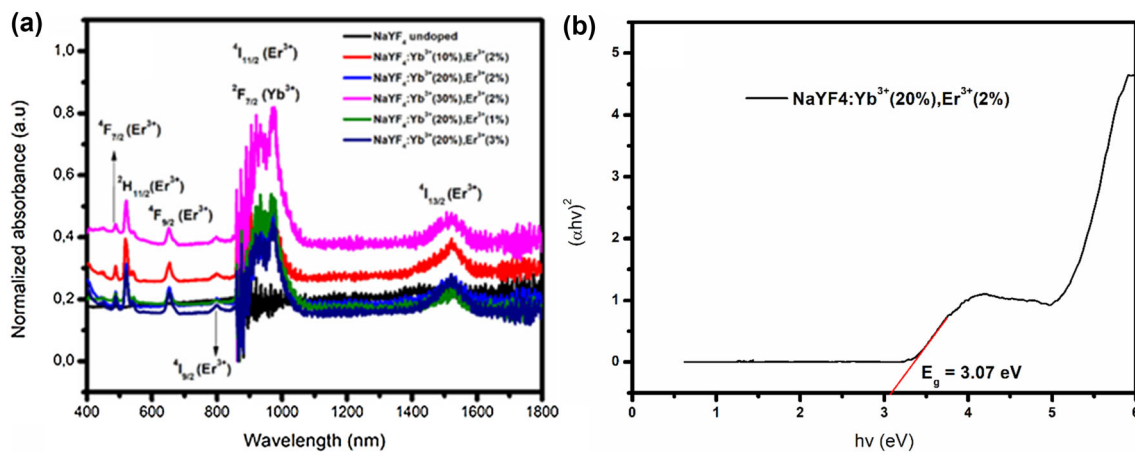
Figure 11. Absorption spectra of (**a**) Yb^{3+}-Er^{3+} co-doped $NaYF_4$ nanocrystals and (**b**) direct bandgap evaluation using Tauc's equation.

density of states of these dopants increases as the doping concentration does, generating a continuum of states that resembles the bands [22]. However, increasing Yb^{3+} ion concentration increases the bandgap. This could be because the bandgap may increase as the concentration increases to the point where it forms a mixed phase material [40]. Annealing the nanocrystals leads to the reduction of their bandgap, which gives the nanocrystals a better chance of being incorporated as the electron transport layer in applications such as perovskite solar cells, where they can absorb low-energy NIR photons and transform them into visible, high-energy light that can be absorbed by perovskite materials to produce more photocurrent. The optical bandgap values were determined for both the undoped, and doped materials based on optical spectrum absorption using the Tauc's relation provided by equation (6) [41]:

$$\alpha h v = A(h v - E_g)^2 \qquad (6)$$

where A is the proportionality constant, α the absorption coefficient and hv the photon energy and E_g is the direct bandgap.

The bandgap of the samples was determined by plotting $(\alpha h v)^2$ as a function of photon energy (hv), and extrapolation of the linear component of the curve to absorption equal to zero, as shown in figure 11b [21,42]. The estimated absorption edge wavelengths and bandgaps for the samples are shown in table 2.

3.6 FTIR and Raman analysis

The vibration modes of molecules in manufactured nanocrystals were studied using FTIR spectroscopy in the wavenumber range of 600 to 2400 cm^{-1} (see figure 12). Figure 12a shows the FTIR spectra of the undoped $NaYF_4$, $NaYF_4$:10%Yb^{3+}, 2%Er^{3+}, $NaYF_4$:20%Yb^{3+}, 2%Er^{3+} and $NaYF_4$:30%Yb^{3+}, 2%Er^{3+} nanocrystals, and figure 12b shows the comparison of the $NaYF_4$:20%Yb^{3+}, 2%Er^{3+} as-

prepared, annealed at 600°C and 700°C. All the samples exhibited the same spectral pattern. The presence of the RE^{3+}–F stretching vibrations in the nanocrystals is confirmed by the peak at ~ 840 cm^{-1} [43]. The peaks at ~ 1073 and 2079 cm^{-1} are assigned to the C–O stretching vibration of the carboxyl groups [44]. The bands at ~ 1360 and 1635 cm^{-1} are attributed to the symmetric and asymmetric stretching vibrations of the carboxylate anions, implying the strong COO–RE^{3+} complex formation on the nanocrystal surface [45]. Figure 12b indicates that increasing the annealing temperature on $NaYF_4$:20%Yb^{3+} and 2%Er^{3+} nanocrystals decrease the band at ~ 1360 cm^{-1}, which can also be an indication of hydroxyl group reduction in the prepared materials.

To discover the non-radiative relaxations, the vibrational modes of the synthesized nanocrystals were studied. The Raman spectra of as-prepared $NaYF_4$:x%Yb^{3+}, 2%Er^{3+} (x = 10, 20 and 30) and $NaYF_4$:20%Yb^{3+}, 2%Er^{3+} annealed at 600 and 700°C are shown in figure 13a–c. The clear and distinct peaks between ~ 150 and 750 cm^{-1} and 1000 cm^{-1} of the hexagonal phase nanocrystals (as-prepared and the $NaYF_4$:20%Yb^{3+}, 2%Er^{3+} annealed at 600°C) are attributable to the lattice of the $NaYF_4$ vibrational characteristics. The vibrational frequencies of the Na-F pair of atoms are assigned to peaks between 460 and 770 cm^{-1}. The presence of the –OH band between 1300 and 1400 cm^{-1} in the as-prepared sample $NaYF_4$:Yb^{3+}(10%),-Er^{3+}(2%) is attributed to Y–OH phonon frequencies. Induced strain could be the cause of the difference in peak intensity [34]. The annealed at 700°C $NaYF_4$:20%Yb^{3+}, 2%Er^{3+} nanocrystals exhibit two dominant broad bands around 366 and 750 cm^{-1}. Upon annealing the sample at 600 and 700°C, the enhancement in the peak intensity and the shifting of the peaks were observed. The chemical bond length of the molecules, which causes electron cloud migration, is linked to the observed shifting of the Raman peaks towards a lower or higher wavenumber. A movement to a higher wavenumber is brought on by a shorter bond

Table 2.   Estimated absorption edge wavelengths and bandgap.

Sample name	Absorbance wavelength (nm)	Estimated bandgap (eV)
As-prepared samples		
NaYF$_4$ undoped	520	3.35
NaYF$_4$:10%Yb^{3+}, 2%Er^{3+}	520	3.62
NaYF$_4$:20%Yb^{3+}, 2%Er^{3+}	520	3.07
NaYF$_4$:30%Yb^{3+}, 2%Er^{3+}	520	5.00
NaYF$_4$:20%Yb^{3+},1%Er^{3+}	520	4.91
NaYF$_4$:20%Yb^{3+},3%Er^{3+}	520	3.36
Annealed @ 600°C		
NaYF$_4$:10%Yb^{3+}, 2%Er^{3+}	520	2.07
NaYF$_4$:20%Yb^{3+}, 2%Er^{3+}	520	3.03
NaYF$_4$:30%Yb^{3+}, 2%Er^{3+}	520	2.89
Annealed @ 700°C		
NaYF$_4$:10%Yb^{3+}, 2%Er^{3+}	520	1.98
NaYF$_4$:20%Yb^{3+}, 2%Er^{3+}	520	2.03
NaYF$_4$:30%Yb^{3+}, 2%Er^{3+}	520	2.01
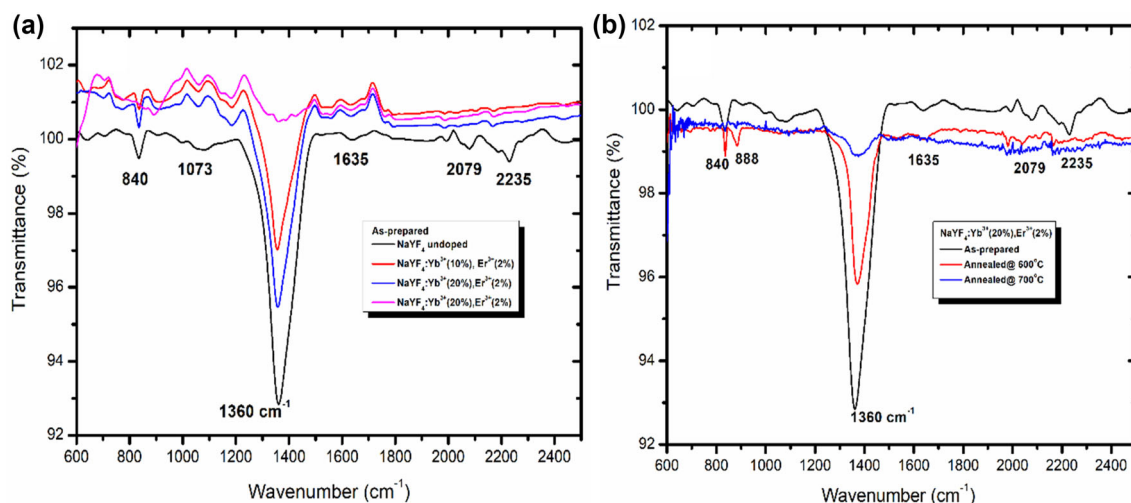
Figure 12.   FTIR spectra of (**a**) as-prepared Yb^{3+}-Er^{3+} co-doped NaYF$_4$ nanocrystals and (**b**) comparison of annealed nanocrystals at 600 and 700°C.

length, whereas a shift to a lower wavenumber is brought on by a longer bond length [45]. Raman spectra confirm the structural behaviour of the synthesized samples. These results support the related XRD data indicating hexagonal and a mixture of hexagonal and cubic phases for the respective nanocrystals.

3.7   TGA analysis

A thermogravimetric (TGA) study was performed to determine the thermal stability and the fraction of volatile components of the NaYF$_4$:20%Yb^{3+}, 2%Er^{3+} nanocrystals by observing the weight change that occurs while the sample is heated at a constant rate. Figure 14 shows the TGA curve of the NaYF$_4$:20%Yb^{3+}, 2%Er^{3+} nanocrystals,

indicating a total weight loss of 10.23% in the temperature region from 20 to 680°C. The initial drop in weight of 3.01% in the range 20–400°C is ascribed to the water loss [46,47]. The evaporation of the nitrates present on the nanocrystals' surface is responsible for the second, more extreme loss of 7.22% in the range 450–680°C [46].

3.8   *Proposed energy-transfer mechanism*

Figure 15 displays the energy levels of the Yb^{3+} and Er^{3+} ions as well as the transfer of energy processes during stimulation at 980 nm. All of the prepared samples exhibit energy transfer up-conversion. The energy transfer up-conversion (ETU) is a UPL by Yb^{3+}-Er^{3+} in which a low-phonon-energy host is needed to prevent the first excited
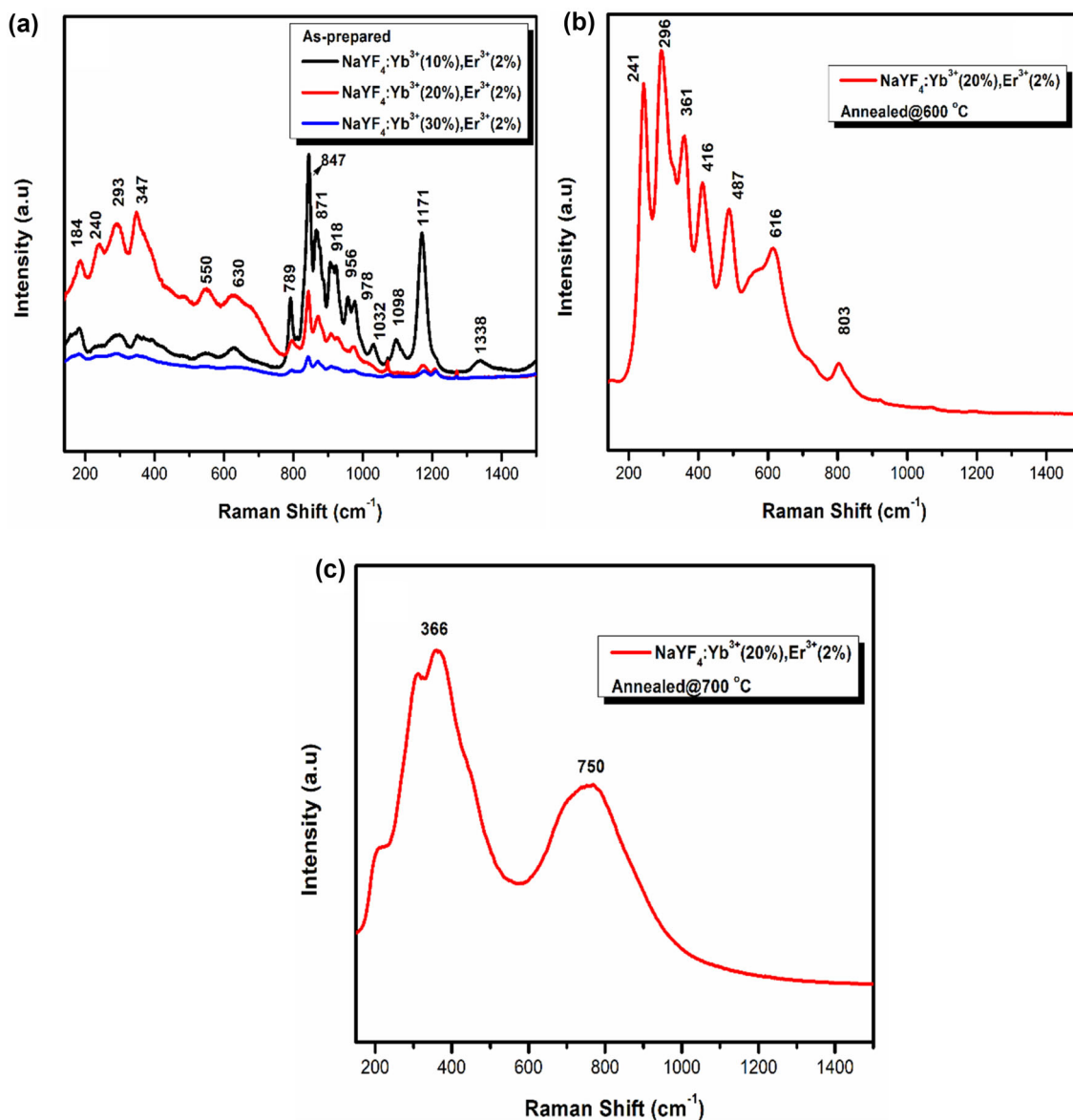
Figure 13. Raman spectra of $NaYF_4$:$10\%Yb^{3+}$, $2\%Er^{3+}$, $NaYF_4$:$20\%Yb^{3+}$, $2\%Er^{3+}$ and $NaYF_4$:$30\%Yb^{3+}$, $2\%Er^{3+}$ nanocrystals: (**a**) as-prepared, (**b**) $NaYF_4$:$20\%Yb^{3+}$, $2\%Er^{3+}$ annealed at 600°C and (**c**) $NaYF_4$:$20\%Yb^{3+}$, $2\%Er^{3+}$ annealed at 700°C.

state (the Er^{3+} $^4I_{11/2}$ level) from rapidly relaxing without emitting radiation. The low phonon energy of $NaYF_4$ accounts for the presence of UPL in these samples [19]. Due to their equal (+3) charge, Yb^{3+} and Er^{3+} ions doped in the $NaYF_4$ host lattice will replace the Y^{3+} site in the $NaYF_4$:Yb,Er mixture. The sequential absorption of two photons in this combination is the foundation of the optical process. As a sensitizer, the Yb^{3+} ion absorbs and transfers NIR photon energy to the Er^{3+} ion in two stages, the excited and intermediate states, respectively. The Er^{3+} ion then experiences multi-phonon relaxations that shift its highly excited states into less excited ones, producing radiative emission in the visible spectrum between 500 and 700 nm [35].

Under 980 nm excitation, the Yb^{3+} ion can be raised from its ground state to the $^2F_{5/2}$ level by the absorption of the first photon, which subsequently transfers the energy to the Er^{3+} ion. In the event that the $^4I_{11/2}$ level is already occupied, this energy transfer can promote the Er^{3+} ion from the $^4I_{15/2}$ level to the $^4I_{11/2}$ level, and from the $^4I_{11/2}$ level to the $^4F_{7/2}$ level via a different energy transfer up-conversion process (or a second 980 nm photon). Green emissions are produced when the Er^{3+} ion relaxes nonradiatively to the $^2H_{9/2}$, $^2H_{11/2}$ and $^4S_{3/2}$ levels ($^2H_{11/2} \rightarrow {}^4I_{15/2}$ and $^4S_{3/2} \rightarrow {}^4I_{15/2}$). If, on the other hand, the ion relaxes even more and occupies the $^4F_{9/2}$ level, red emission ($^4F_{9/2} \rightarrow {}^4I_{15/2}$) results [17]. Through a two-photon UC process, the dominant green and red emissions are observed by these
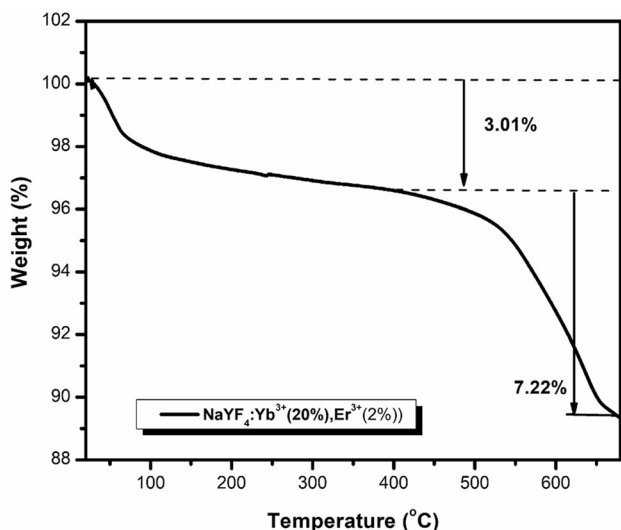
Figure 14. Thermogravimetric analysis curves of NaYF$_4$:20%-Yb^{3+}, 2%Er^{3+} nanocrystals.
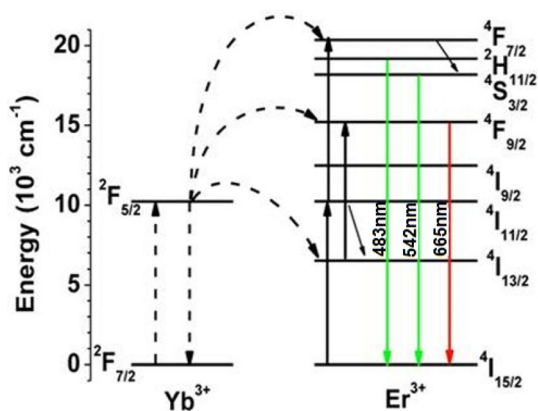
Figure 15. Mechanism of Yb^{3+} to Er^{3+} energy transfer under stimulation at 980 nm.

transitions from the previously stated states to $^4I_{15/2}$ level [48]. According to these findings, the reemission of a photon following the absorption of a photon occurs at a higher energy level than the initial excitation energy. As a result, up-conversion, which makes use of multi-photon absorption to convert NIR excitation into visible light, was observed.

4. Conclusion

NaYF$_4$:Yb^{3+}, Er^{3+} nanocrystals were successfully prepared by the combustion method in the presence of urea as a combustion fuel, and the influence of the concentration of the dopants and the annealing temperature on the structure, morphology and optical properties were examined. The NaYF$_4$:Yb^{3+}, Er^{3+} nanocrystals were annealed at 600 and 700°C, respectively. The XRD analysis

indicated the hexagonal phase for the as-prepared and nanocrystals annealed at 600°C and the cubic phase for the 700°C annealed nanocrystals. Diffraction patterns of the nanocrystals showed the impurity peaks, which may have been caused by the rapid reaction times of the nanocrystals. The nanocrystals demonstrated different morphologies, including spherical, cubic, hexagonal and porous, as dopant concentrations (10–30 mol% of Yb^{3+}, 1–3 mol% of Er^{3+}) and annealing temperatures were changed. The UPL analysis indicated the efficient energy transfer from Yb^{3+} to Er^{3+} when the Yb^{3+} concentration was increased from 10 to 20% and showed concentration quenching when Yb^{3+} was increased to 30%. Two green and one red up-conversion emissions centred at ∼483, 542 and 665 nm attributed to $^2H_{11/2} \rightarrow {}^4I_{15/2}$, $^4S_{3/2} \rightarrow {}^4I_{15/2}$ and $^4F_{9/2} \rightarrow {}^4I_{15/2}$ transitions of erbium, respectively, were observed under 980 nm laser excitation for all Yb^{3+}-Er^{3+} co-doped NaYF$_4$ samples. Annealing the nanocrystals showed an improvement in the up-conversion luminescence intensities from UPL analysis. The UV–Vis analysis of the samples revealed that the nanocrystals exhibit six characteristics peaks centred at ∼487, 520, 654, 802, 972 and 1526 nm ascribed to $^4I_{15/2} \rightarrow {}^4F_{7/2}$ (∼487 nm), $^4I_{15/2} \rightarrow {}^4H_{11/2}$ (∼520 nm), $^4I_{15/2} \rightarrow {}^2F_{9/2}$ (∼654 nm), $^4I_{15/2} \rightarrow {}^4I_{9/2}$ (∼802 nm), $^4I_{15/2} \rightarrow {}^4I_{11/2}$ (∼972) and $^4I_{15/2} \rightarrow {}^4I_{13/2}$ (∼1500 nm) transitions of Er^{3+}, respectively. The absorption peak at ∼972 nm attributed to the $^2F_{7/2}$ transition of Yb^{3+} overlaps with the $^4I_{11/2}$ absorption transition of Er^{3+}. The UV–Vis absorption spectra indicated that both Er and Yb are well incorporated into the lattice of NaYF$_4$. FTIR spectra showed the expected vibrational modes of the NaYF$_4$:Yb^{3+},Er^{3+} nanocrystals, and the Raman spectra revealed the clear and distinct peaks between 150 and 750 cm^{-1}, and 1000 cm^{-1} of the hexagonal phase nanocrystals (as-prepared and the NaYF$_4$:20%Yb^{3+}, 2%Er^{3+} annealed at 600°C), which were attributed to the host lattice NaYF$_4$ vibrational characteristics. Upon annealing the samples at 600 and 700°C, the enhancement in the peak intensity and also the shifting of the peaks was observed. The Raman analysis was in good agreement with the XRD data. TGA confirmed the thermal stability of the NaYF$_4$:20%Yb^{3+}, 2%Er^{3+} sample with two weight losses of 3.01 and 7.22% in the wave ranges of 20–400 and 450–680°C, respectively, assigned to the water loss and the evaporation of the nitrate ions. The proposed energy transfer mechanism suggests an energy transfer from Yb^{3+} to Er^{3+} ions, and UPL confirmed this phenomenon. The prepared materials were analysed for applications in optical devices and solar cells, and we can conclude that with a careful variation of sensitizer-activator doping concentration and thermal treatment, these materials stand a good chance of serving as both light intensity amplifiers and photon absorption efficiency enhancers in optical devices and perovskite solar cells, respectively.

Acknowledgements

References

[1] John R and Rajakumari R 2012 *Nano-Micro Lett.* **4** 65

[2] Sharma N, Jandaik S, Singh T G and Kumar S 2016 *Nanobiomater. Antimicrob. Ther.* **6** 483

[3] Mbule P, Mlotswa D, Mothudi B and Dhlamini M 2021 *J. Luminesc.* **235** 118060

[4] Ntwaeaborwa O M, Mofokeng S J, Kumar V and Kroon R E 2017 Spectrochim. *Acta Part A: Mol. Biomol. Spectrosc.* **182** 42

[5] Ma D K, Huang S M, Yu Y Y, Xu Y F and Dong Y Q 2009 *J. Phys. Chem. C* **113** 8136

[6] Lim S F and Austin R H 2015 In: *Applications of nanoscience in photomedicine* (Chandos Publishing) 377

[7] Schäfer H, Ptacek P, Kömpe K and Haase M 2007 *Chem. Mater.* **19** 1396

[8] Wilhelm S, Hirsch T, Patterson W M, Scheucher E, Mayr T and Wolfbeis O S 2013 *Theranostics* **3** 239

[9] Wang L and Li Y 2007 *Chem. Mater.* **19** 727

[10] Talane T E 2017 *Study of structural and optical properties of undoped and rare earth doped TiO₂ nanostructures* (PhD thesis)

[11] Sharma R K, Mudring A V and Ghosh P 2017 *J. Luminesc.* **189** 44

[12] Chen J and Zhao J X 2012 *Sensors* **12** 2414

[13] Solís D 2010 *Up-converted luminescent properties of rare-earth doped ZrO₂ nanocrystals* (Phd thesis)

[14] Vidyakina A A, Kolesnikov I E, Bogachev N A, Skripkin M Y, Tumkin I I, Lähderanta E *et al* 2020 *Materials* **13** 3397

[15] Pellegrino A L 2019 *Synthesis of hybrid metalorganic/inorganic systems and doped halide thin films for photovoltaics* (PhD thesis) Universita decli Studi Di Catania)

[16] Kavand A, Serra C A, Blanck C, Lenertz M, Anton N, Vandamme T *et al* 2021 *ACS Appl. Nano Mater.* **4**(5) 5319

[17] Shan S N, Wang X Y and Jia N Q 2011 *Nanoscale Res. Lett.* **6** 1

[18] Sharma R K and Ghosh P 2021 *Front. Chem.* **9** 580

[19] Hakmeh N, Chlique C, Merdrignac-Conanec O, Fan B, Cheviré F, Zhang X *et al* 2015 *J. Solid State Chem.* **226** 255

[20] Roh J, Yu H and Jang J 2016 *ACS Appl. Mater. Interfaces* **8** 19847

[21] Huang Q, Ye W, Jiao X, Yu L, Liu Y and Liu X 2018 *J. Alloys Compd.* **763** 216

[22] He S, Xia H, Zhang J, Zhu Y and Chen B 2017 *Sci. Rep.* **7** 1

[23] Kaiser M 2021 *Upconversion quantum yield and luminescence of beta-NaYF4: Yb3+, Er3+ nanoparticles* PhD Thesis (Technischen Universität Berlin)

[24] Blake A J, Cole J M, Evans J S, Main P, Parsons S and Watkin D J 2009 *Crystal structure analysis: principles and practice* (Vol. 13) OUP Oxford

[25] Bamidele E 2022 Re: *What are all possible reasons for the peak shift in X-Ray Diffraction?* Retrieved from: https://www.researchgate.net/post/What-are-all-possible-reasons-for-the-peak-shift-in-X-RayDiffraction/635b61866a718dd856070a8b/citation/download

[26] Rozkuszka K P 1977 *High-pressure x-ray diffraction study of linear polyethylene* PhD Thesis (University of Massachusetts Amherst)

[27] Stanev V, Vesselinov V V, Kusne A G, Antoszewski G, Takeuchi I and Alexandrov B S 2018 *NPJ Comput. Mater.* **4** 1

[28] Srinet G, Sharma S, Guerrero-Sanchez J, Garcia-Diaz R, Ponce-Perez R, Siqueiros J M *et al* 2020 *J. Alloys Compd.* **849** 156587

[29] Karamat S, Rawat R S, Lee P, Tan T L and Ramanujan R V 2014 *Prog. Nat. Sci.: Mater. Int.* **24** 142

[30] Cheng W and Ma X 2009 *J. Phys.: Conf. Series* (Vol. 152, No. 1, p. 012039) IOP Publishing

[31] Mbule P S 2013 *The effects of the ZnO nanoparticles buffer layer on organic solar cells* Phd thesis (University of the Free State)

[32] Lekesi L P, Motaung T E, Motloung S V, Koao L F and Malevu T D 2022 *J. Mol. Struct.* **1251** 132014

[33] Ali D, Butt M Z, Muneer I, Farrukh M A, Aftab M, Saleem M *et al* 2019 *Thin Solid Films* **679** 86

[34] Samsonov D, Zhdanov S, Morfill G and Steinberg V 2003 *New J. Phys.* **5** 24

[35] Namagal S, Jaya N V, Muralidharan M and Sumithra S 2020 *J. Mater. Sci.: Mater. Electron.* **31** 11398

[36] Nagli L, Gaft M, Fleger Y and Rosenbluh M 2008 *Opt. Mater.* **30** 1747

[37] Wen S, Zhou J, Zheng K, Bednarkiewicz A, Liu X and Jin D 2018 *Nat. Commun.* **9** 1

[38] Alkahtani M, Almuqhim A A, Qasem H, Alsofyani N, Alfahd A, Alenzi S M *et al* 2021 *Nanomater.* **11** 2909

[39] Wang Q, Tan M C, Zhuo R, Kumar G A and Riman R E 2010 *Nanosci. Nanotechnol.* **10** 1

[40] Shaker A and Zekry A 2010 *J. Electron Dev.* **8** 293

[41] Mbule P S 2013 *The effects of the ZnO nanoparticles buffer layer on organic solar cells* Phd thesis (University of the Free State)

[42] Huang Y 2017 *Upconverting nanoparticles for integration in bioimaging and therapeutic applications* Phd thesis (Université du Québec, Institut national de la recherche scientifique)

[43] Giang L T K, Trejgis K, Marciniak L, Vu N and Minh L Q 2020 *Sci. Rep.* **10** 1

[44] Zhao P, Wu Y, Zhu Y, Yang X, Jiang X, Xiao J *et al* 2014 *Nanoscale* **6** 3804

[45] Wan F, Shi H, Chen W, Gu Z, Du L, Wang P *et al* 2017 *Nanomaterials* **7** 210

[46] Li Z, Miao H, Fu Y, Liu Y, Zhang R and Tang B 2016 *Nanoscale Res. Lett.* **11** 1

[47] Kawai K, Fukuda T, Nakano Y and Takeshita K 2016 *EPJ Nuclear Sci. Technol.* **2** 44

[48] Ding M, Chen D, Yin S, Ji Z, Zhong J, Ni Y, Lu C and Xu Z 2015 *Sci. Rep.* **5** 1